


Multiphysics Sizing of Interior Permanent Magnet Machines Based on Geometric Methodology

MOSTAFA AHMADI DARMANI ¹, ANDREA CAVAGNINO ² (Fellow, IEEE),
SILVIO VASCHETTO ² (Senior Member, IEEE), FABRIZIO MARGINETTI ³ (Senior Member, IEEE),
AND CHRISTOPHER GERADA ¹ (Senior Member, IEEE)

¹Power Electronics, Machines and Control Group, the University of Nottingham, NG7 2RD Nottingham, U.K.

²Dipartimento Energia, Politecnico di Torino, 10129 Turin, Italy

³University of Cassino and South Lazio, 03043 Cassino, Italy

CORRESPONDING AUTHOR: MOSTAFA AHMADI DARMANI(email: mostafa.ahmadi@nottingham.ac.uk).

ABSTRACT This study presents a sizing methodology in the frame of the multidisciplinary design of interior permanent magnet synchronous machines. The proposed approach targets at obtaining an initial electromagnetic design of the machine, including diameters, axial length, rotor barrier shape, stator slot geometry as well as the winding layout. The analytical design workflow consists of an iterative sizing procedure based on a robust geometric model, consistent equations, and no correction factors. The process is carried out starting from very basic design parameters such as rated voltage, torque, and magnetic material properties. The modular structure of the proposed design algorithm can be easily integrated with optimization routines obtaining a final optimized design, which contemplates various multiobjective constraints.

INDEX TERMS Air gap flux density, electromagnetic sizing, equivalent ring method, finite element, interior permanent magnet (IPM) machine, lumped parameter thermal network, magnetic equivalent circuit (MEC), magnetic field, mechanical stress, multiphysics modeling, synchronous machine, winding function theory.

I. INTRODUCTION

INTERIOR permanent magnet (IPM) synchronous machine is one of the most popular topologies effectively served for high-performance electric motors applications. This technology offers to a diverse array of requirements, encompassing a wide constant-power speed range, exceptional efficiency, high power and torque density, compared to the conventional asynchronous configuration [1]. Its versatility makes it an ideal choice for various sectors, including domestic appliances, hybrid / electric vehicle propulsion systems, wind turbines, and aircraft applications.

The torque generation in IPM machines results from their inherent anisotropic structure and relies on two components, namely the reluctance and PM torque. The key features of IPM machines are enhanced torque density, more robust rotor structure, and higher irreversible demagnetization tolerance compared to conventional isotropic surface-mounted PM machines [2], [3]. Among several introduced IPM architectures,

V- shape IPM machines exhibit higher torque densities than other topologies [4].

Traditionally, electrical machines are designed on the basis of simple analytical equations taking into account some design considerations according to the designer experience and approximated working temperatures of different machine parts (winding and magnets). Such a design approach may be acceptable for machines having simple isotropic structures such as surface-mounted PM machines, while it presents significant challenges for the IPM machines, in particular at the initial sizing step. This complexity arises from the intricate electromagnetic modeling of heavily saturated rotor regions and the substantial leakage flux that traverses through ribs or iron bridges [5]. As a result, accurately predicting the air gap flux density distribution is demanded with the use of sophisticated techniques, such as subdomain model [6], [7], [8], magnetic equivalent circuit (MEC) [9], [10], and numerical finite element method (FEM) [11].

The subdomain model, MEC, and FEM each offer advantages and limitations for the design and modeling of electrical machines. The subdomain model is efficient and less computationally demanding, making it suitable for early-stage design, but it lacks the precision needed for complex geometries and nonlinear materials. The magnetic equivalent circuit is highly intuitive and allows for rapid evaluations, providing a simplified representation of the machine's behavior. Although it might initially oversimplify the physical problem, this limitation can be addressed by refining the network with more detailed elements and increasing the number of reluctances. Additionally, incorporating the nonlinear behavior of materials can enhance its accuracy, making the method more robust for detailed magnetic analysis. On the other hand, FEM offers high accuracy and comprehensive analysis capabilities, handling complex geometries and non-linear phenomena effectively, but at the cost of significant computational resources and time. Given these considerations, the magnetic equivalent circuit can be particularly advantageous for the design phase due to its balance of simplicity, speed, and flexibility, making it an efficient tool for design and iterative adjustments, facilitating an efficient exploration of the design space.

Generally, bilateral or central bridges should be a tradeoff to ensure electromagnetic performance and structural reliability [12], [13], [14], [15]. Thus, a pragmatic yet accurate design methodology is required which takes into consideration electromagnetic, thermal and structural physical aspects [13].

Most studies on electrical machines have concentrated on their electromagnetic design and modeling, often neglecting thermal and mechanical aspects. However, there is a growing interest in employing a multiphysics approach to enhance the overall design and performance of these machines. For instance, several studies have integrated parametric FEM electromagnetic models, thermal networks, and analytical structural solutions to optimize designs, such as surface-mounted PM synchronous machines, and IPM V-shaped machines. These studies highlight the importance of considering mechanical stress and cooling systems alongside electromagnetic performance. While FEM is favored for its accuracy, the process can be time-consuming, especially for optimization and sensitivity analysis.

An analytical approach was used to model a multiphysics IPM machine for compressor applications [16]. This modeling incorporated all the physical aspects of the machine. The electromagnetic part was represented by an equivalent $d-q$ machine based on flux density waveforms in the different axes of the $d-q$ frame. Additionally, a steady-state thermal model was employed to account for thermal resistance and heat sources. Various loss components were considered, and their thermal effects were applied to the materials. The mechanical model included calculations for centrifugal force, mechanical stresses, and both static and dynamic deformations. These models were integrated for design optimization, resulting in a Pareto front of efficiency and weight of the machine.

A multiobjective and multiphysics design for a double V-shaped IPM machine was proposed, incorporating analytical

designs for the electromagnetic, thermal, and structural components [9]. The electromagnetic design relied on a nonlinear analytical model, Ampere's theorem, and the flux conservation law, with details provided in [17]. This approach considered local saturation near the iron bridge, slot tangential leakage flux, and winding leakage flux. The accuracy of this method closely matched results obtained from FEM simulations, despite its complexity.

A multiphysics model for a PM synchronous machine used in traction applications was presented in [18]. The electromagnetic and thermal aspects were represented by a lumped model, while the vibro-acoustic and mechanical parts were analyzed using analytical equations. The proposed model was verified through numerical FEM simulations and experimental tests, with acceptable accuracy.

A comprehensive analytical-based multiphysics model for an IPM machine was detailed in papers [19] and [20]. This model used a mesh-MEC, a lumped parameter thermal network, and a mechanical model for the respective electromagnetic, thermal, and mechanical aspects. The mechanical model was particularly advanced, utilizing a four-node two-dimensional (2-D) isoparametric quadrilateral element with 2 degrees of freedom per node in the X and Y directions, which allowed for elements with curved sides suitable for cylindrical structures. This model could perform modal analysis, structural harmonic analysis, and acoustic analysis, with excellent agreement between the analytical model and FEM simulations. This approach is applicable to the predesign and modelling of electrical machines. A similar methodology for designing a V-shape IPM machine was also proposed in papers [10], [21].

A hybrid magnetic equivalent circuit model was used for the electromagnetic design, facilitating rapid computation. Due to potential mechanical issues with thin bridges, maximum shear stress in the inner and outer bridges was evaluated during the design process. Additionally, a lumped parameter thermal network was employed to predict temperatures in different machine parts. FEA was used to validate the methodology, although the study neglected rotor pole saturation and rotor iron loss, which could lead to some inaccuracies in the final results.

A. PAPER NOVELTY AND AIMS

This article proposes a simple, effective, and highly rapid design technique for V-type interior permanent magnet (IPM) machines, distinguished by several innovative aspects. The proposed methodology introduces a unique geometric perspective to the initial design phase of IPM machines. By focusing on optimizing geometric parameters such as diameters, axial length, rotor barrier shape, stator slot geometry, and winding layout, our approach offers a more intuitive understanding of how these parameters influence machine performance. This geometric-centric methodology facilitates faster and more accurate initial designs, setting it apart from conventional methods that may not emphasize geometric considerations as strongly. Additionally, we integrate FEA-fixed

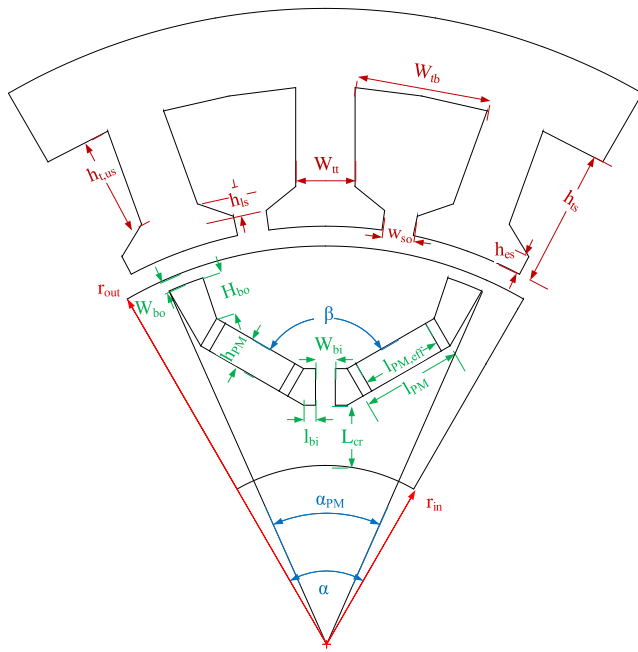


FIGURE 1. Geometric parameters of the machine.

technique is integrated with predetermined mechanical stress constraints. This ensures that the resulting designs not only meet electromagnetic performance targets but also hold to mechanical durability requirements, addressing a critical gap in existing design methodologies where mechanical and electromagnetic aspects are often treated separately. Furthermore, this study presents an innovative multiphysics sizing approach that combines electromagnetic, thermal, and mechanical considerations. Unlike traditional design methods that typically treat these aspects in isolation, our holistic integration leads to a more cohesive and efficient design process. The effectiveness of the proposed sizing strategy has been verified through the design of numerous IPM machines, validated using FEA software. These unique contributions collectively enhance the design process of IPM machines, offering a more efficient, accurate, and robust methodology.

II. GEOMETRICAL MODELLING OF V-SHAPE IPM MACHINES

Evaluating the electromagnetic and mechanical characteristics of an IPM machine requires a consistent geometric model. Fig. 1 shows a comprehensive model of an IPM machine consisting of the one pole. The latter is comprised of two magnet pieces arranged in a V-configuration, and the number of stator slots can be selected depending on the winding design.

The external radius of the stator r_{ex} can be determined by considering the slot dimensions and the length of the stator back-iron as follows:

$$r_{ex} = r_{out} + g + h_{es} + h_{ts} + h_{t,us} + L_{cs} \quad (1)$$

where h_{es} , h_{ts} , and $h_{t,us}$ are the stator slot dimensions as specified in Fig. 1 and L_{cs} is the length of the stator back-iron. These dimensions are further elaborated upon in papers [22], [23], and [24], which provides comprehensive insights into the procedure for calculating various stator parameters.

In this model, the rotor is parametrized by imposing the following quantities: the magnet polar pitch ratio α , the angle between two magnets or V-angle β , the magnet thickness h_{pm} , the radial extension of the outermost part of the barrier H_{bo} , the tangential extension of the innermost part barrier l_{bi} , and the magnet fill factor $K_{fill,PM}$. The remaining parameters of the rotor can be calculated easily. It is worth mentioning that the geometric variables H_{bo} , l_{bi} , and $K_{fill,PM}$ have been established to provide more degree of freedom to the model. These parameters can be neutralized, setting H_{bo} and l_{bi} equal to zero and $K_{fill,PM}$ equal to one.

The angular magnetic pole, represented α_{PM} as shown in Fig. 1 is computed as follows:

$$\alpha = \frac{2\pi}{P} \quad (2)$$

$$\alpha_{PM} = k_{PM}\alpha \quad (3)$$

where P is the number of poles, k_{PM} is the ratio of PM pole to pole pitch, so-called magnet polar pitch. Theoretically, this ratio can be defined between 0 and 1, but its practical value is in the range 0.7–0.85. The inert region of the rotor with a radius smaller than r_{in} , mechanically transfers torque from the rotor to the shaft. It is frequently simply an extension of the rotor yoke, or it can be a lightweight material.

In V-type IPM machines, the length of rotor back iron L_{cr} is mainly considered for mechanical purposes, and it has no impact on the electromagnetic performance of the machine. So, a very thin length can be taken into consideration in order only to satisfy the mechanical performance of the rotor. However, this geometrical parameter should be calculated on the basis of maximum permissible flux density when β is relatively high. Also, L_{cr} should be sized on the basis of maximum allowable flux when β is higher than 170° since the majority of the flux goes through the rotor back iron. In this circumstance, the rotor back iron should not only guarantee the mechanical performance, but also it should be thick enough to allow the flux to pass through the rotor back iron. Small values of L_{cr} may lead to highly loaded regions or saturation in the rotor back iron and consequently deteriorate the electromagnetic performance of the machine.

The area between the inner radius of the rotor r_{in} and the outer radius of the rotor r_{out} is considered the active part of the rotor where the flux barriers and magnets are placed. Conventionally, flux barriers are implemented to prevent the flowing of the magnetic flux between two adjacent magnets in the rotor. Besides, they can retain the magnets firmly inside the rotor structure and protect them against mechanical forces and tensions. These cavities cause high rotor anisotropy and have a significant impact on the electromagnetic behavior of

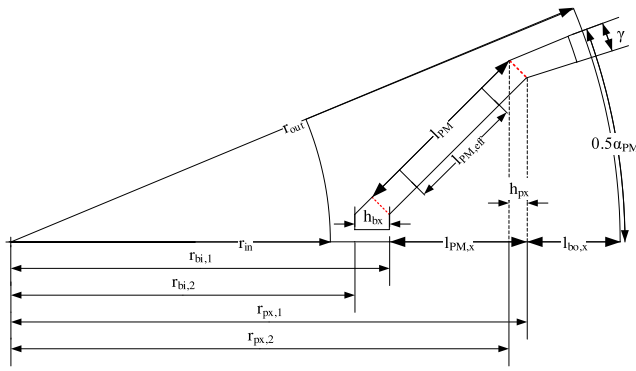


FIGURE 2. Representation of geometric parameters of barrier and magnet.

the machine. Basically, rotor anisotropy can change the distribution of magnetic flux density in the air gap, affecting the torque value and its profile, loss and consequently efficiency, and irreversible demagnetization of the magnets placed in the rotor. Furthermore, rotor anisotropy introduces variation of reluctances and accordingly inductance variation along direct and quadrature axes. Therefore, an appropriate shape design can improve the torque and power density and reduce the iron losses and torque ripple, enhance the machine efficiency, and mitigate irreversible demagnetization.

In order to provide a highly flexible flux barrier's shape, two geometric parameters, l_{bi} and H_{bo} , are defined to extend the innermost part of cavities tangentially and the outermost part of the cavities radially, respectively. The designer can specify these geometric parameters for the manufacturing purpose. Also, they can be calculated by means of an optimization process to enhance the output torque and reduce the torque ripple [25].

Fig. 2 illustrates the half of the rotor pole including flux barriers and magnet dimensions. Knowing the outer radius of rotor and extension lengths of flux barrier and magnet thickness, it is possible to calculate the length of the magnet l_{PM}

$$W_b = \frac{W_{bi}}{2} + l_{bi} \quad (4)$$

$$r_{bo} = r_{out} - W_{bo} \quad (5)$$

$$r_{bi,1} = r_{bo} \left(\cos(\alpha_{PM} - \gamma) - \frac{\sin(\alpha_{PM} - \gamma)}{\tan\left(\frac{\beta}{2}\right)} \right) + \frac{W_b}{2 \tan\left(\frac{\beta}{2}\right)} \quad (6)$$

$$h_{bx} = \frac{h_{PM}}{\sin\left(\frac{\beta}{2}\right)} \quad (7)$$

$$r_{bi,2} = r_{bi,1} - h_{bx} \quad (8)$$

$$r_{px,1} = \frac{r_{bo} \frac{\sin(\alpha_{PM} - \gamma)}{\cos(\alpha)} - r_{bi,2} \tan\left(\frac{\beta}{2}\right) + \frac{W_b}{2}}{\tan(\alpha) - \tan\left(\frac{\beta}{2}\right)} \quad (9)$$

$$h_{px} = h_{PM} \sin\left(\frac{\beta}{2}\right) \quad (10)$$

$$r_{px,2} = r_{px,1} - h_{px} \quad (11)$$

$$l_{PM,x} = r_{px,1} - r_{bi,1} \quad (12)$$

$$l_{bo,x} = r_{out} - r_{px,1} \quad (13)$$

$$l_{PM} = \sqrt{(r_{px,2} - r_{bi,1})^2 + \left(\frac{(r_{px,1} - r_{bi,2}) \tan\left(\frac{\beta}{2}\right) - h_{PM} \cos\left(\frac{\beta}{2}\right)}{1} \right)^2} \quad (14)$$

Additionally, a fill factor coefficient that acts on the length of magnet is defined to take into account some of the manufacturing constraints, such as magnet segmentation. It should be remarked that the thickness of internal W_{bi} and bilateral W_{bo} bridges should be determined on the basis of mechanical considerations including the maximum rotating speed of the machine and mechanical properties of rotor core material. The mechanical modeling should be performed subsequently to geometry acquisition and preceding electromagnetic modelling. This sequence ensures the validation of rotor geometry from a structural perspective. Such validation is pivotal in ensuring a design that is both realistic and reliable. The following section elaborates on the mechanical modelling of the rotor.

III. MECHANICAL DESIGN AND STRESS CALCULATION

The geometry of flux barriers (i.e., the thickness of bilateral and central bridges) has a diverse behavior from the electromagnetic and mechanical viewpoint. A very thin bridge can save a lot of generated magnetic flux by magnets, but it is not appropriate to form structural viewpoint since it may not withstand the high mechanical stress developed on the narrow areas of the bridges increasing the risk of deformation and failure [26], [27]. It is worth to mention that soft magnetic materials, specifically laminated steels, which have a degree of ductility, allowing them to withstand deformation when subjected to high stress. This deformation can either be elastic, where the material returns to its original shape after force is removed, or plastic, wherein the material remains deformed even after the force is removed. On the other hand, PMs are brittle, and any deformation they undergo is exclusively elastic in nature. Consequently, it is mandatory to avoid any instance of plastic deformation, regardless of the circumstances, or the PMs will break immediately when they are loaded over their maximum mechanical stress [28], [29].

Usually, safety factors are taken into consideration during the design procedure to prevent the failure of both soft and hard magnetic materials and improve the reliability of the machine. However, these factors applied alone are insufficient to guarantee the safe operation of the machine. For instance, cyclic loads and fatigue lead to the ageing of the materials and consequently change the mechanical characteristics of the materials [30].

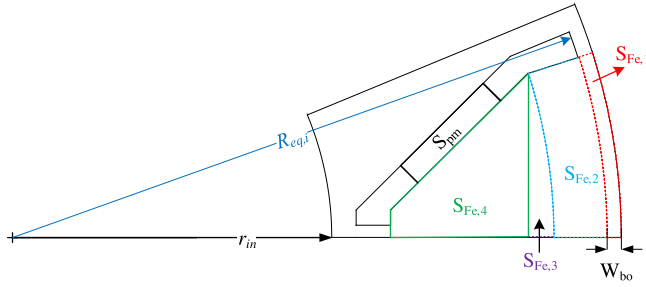


FIGURE 3. Mechanical model of IPM machine.

Generally, two methodologies can be employed to calculate the stress exerted on the tangential and bilateral bridges. The first method involves accurate numerical FEM simulation, which calculate the Von Mises stress at the maximum rotational speed. Although accurate, this method is relatively time-consuming. The second technique employs simplified analytical techniques like the equivalent ring method [31] and beam theory [15], [32] calculating centrifugal and tangential forces.

These methods calculate centrifugal and tangential forces, offering quicker results sounding more appealing at the initial design stage [33].

A. EQUIVALENT RING METHOD

The equivalent ring method might be the most well-known technique to analytically calculate the mechanical stress on the sleeve and bilateral bridges in high-speed PM machines. This technique transforms the centrifugal force acting on the rotor pole and magnets into a thin ring. The ring is as thick as the tangential bridges, and its mass density is calculated to maintain the centroid of the pole section and magnets as well.

In V-shape IPM machines, the angle between the magnets β is an essential parameter which has a great impact on the electromagnetic and mechanical behavior of the machine. From the structural standpoint, small values of β can decrease the centroid radius of rotor and magnets and consequently leads to lower stress values on the iron bridges. Fig. 3 represents a half-pole centroid model of the V-shape rotor. As seen, the pole is divided into two parts, the iron areas defined as $S_{Fe,i}$ and the magnet area defined as S_{pm}

$$r_{eq,i} = r_{out} - W_{bo} \quad (15)$$

where $r_{eq,i}$ is the inner radius of the equivalent ring, and the outer radius of the equivalent ring is equal to the outer radius of the rotor r_{out} .

Basically, the centroid of the rotor can be defined in the radial and axial directions. In order to enhance the computational efficiency, it is possible to disregard the axial centroid in the calculation procedure, owing to the inherent cylindrical and uniform attributes of the rotor. Therefore, solely the centroid pertaining to the radial direction is taken into account.

The centroid radius of geometry can be expressed as follows:

$$\begin{cases} X_{cent} = \frac{\sum_i \iint_{D_i} x d\sigma_i}{\sum_i A_{S_i}} \\ Y_{cent} = \frac{\sum_i \iint_{D_i} y d\sigma_i}{\sum_i A_{S_i}} \end{cases} \quad (16)$$

$$R_{cent} = \sqrt{X_{cent}^2 + Y_{cent}^2} \quad (17)$$

Considering the symmetrical nature of the rotor structure, centroid in vertical axis is equal to zero in equation:

$$R_{cent} = \sqrt{X_{cent}^2 + 0} = X_{cent} \quad (18)$$

To calculate the X_{cent} , the centroid of magnet and rotor pole shoe sections shown in Fig. 3 should be calculated. The centroid of the magnet can be expressed as follows:

$$\begin{aligned} R_{c,PM} = r_{eq,i} \cos\left(\frac{\alpha_{pm}}{2}\right) - r_{eq,i} \frac{\sin\left(\frac{\alpha_{pm}}{2}\right)}{\tan\left(\frac{\beta}{2}\right)} - \frac{h_{pm}}{2 \sin\left(\frac{\alpha_{pm}}{2}\right)} \\ + \cos\left(\frac{\alpha_{pm}}{2}\right) \left(\frac{h_{pm}}{2 \tan\left(\frac{\beta}{2}\right)} + h_{pm} + \frac{l_{pm}}{2} \right). \end{aligned} \quad (19)$$

The centroid of four iron sections can be given as follows:

$$R_{cent,Fe} = \sum_{k=1,2,3,4} \frac{\int \int_{S_{Fe,k}} x d\sigma_{Fe,k}}{A_{Fe,k}} \quad (20)$$

$$\int \int_{S_{Fe,1}} x d\sigma_{Fe,1} = \frac{2}{3} (r_{out}^3 - r_{eq,i}^3) \sin\left(\frac{\alpha_{pm}}{2} - \gamma\right) \quad (21)$$

$$\int \int_{S_{Fe,2}} x d\sigma_{Fe,2} = \frac{2}{3} (r_{eq,i}^3 - (r_{eq} - H_{bo})^3) \sin\left(\frac{\alpha_{pm}}{2} - \gamma\right) \quad (22)$$

$$\begin{aligned} \int \int_{S_{Fe,3}} x d\sigma_{Fe,3} = \frac{2}{3} r_{eq,i}^3 \left(\sin\left(\frac{\alpha_{pm}}{2} - \gamma\right) - \cos^3\left(\frac{\alpha_{pm}}{2} - \gamma\right) \right. \\ \left. \times \tan\left(\frac{\alpha_{pm}}{2} - \gamma\right) \right) \end{aligned} \quad (23)$$

$$\begin{aligned} \int \int_{S_{Fe,4}} x d\sigma_{Fe,4} \approx r_{eq,i}^3 \left(\sin^2\left(\frac{\alpha_{pm}}{2} - \gamma\right) \times \frac{\cos\left(\frac{\alpha_{pm}}{2} - \gamma\right)}{\tan\left(\frac{\beta}{2}\right)} \right. \\ \left. - \frac{\sin^3\left(\frac{\alpha_{pm}}{2} - \gamma\right)}{3 \tan^2\left(\frac{\beta}{2}\right)} \right) \end{aligned} \quad (24)$$

$$A_{Fe,1} = (\alpha_{pm} - 2\gamma) (r_{out}^2 - r_{eq,i}^2) \quad (25)$$

$$A_{Fe,2} = (\alpha_{pm} - 2\gamma) (r_{eq,i}^2 - (r_{eq,i} - H_{bo})^2) \quad (26)$$

$$\begin{aligned} A_{Fe,3} = \frac{1}{2} (r_{eq,i} - H_{bo})^2 \left(\frac{\alpha_{pm}}{2} - \gamma \right. \\ \left. - \sin\left(\frac{\alpha_{pm}}{2} - \gamma\right) \right) \end{aligned} \quad (27)$$

$$A_{Fe,4} = (r_{eq,i} - H_{bo})^2 \sin^2 \left(\frac{\alpha_{pm}}{2} - \gamma \right) \tan \left(\frac{\beta}{2} \right). \quad (28)$$

Knowing the centroid of the rotor pole and magnets, it is possible to determine the equivalent mass density of the ring

$$\rho_{eq} = \left(\frac{2R_{cent,PM}\rho_{PM}A_{PM} + R_{cent,Fe}\rho_{Fe}A_{Fe}}{2A_{ring}R_{ring}} \right) \times \left(1 - \cos \left(\frac{\alpha_{pm}}{2} - \gamma \right) \right) \quad (29)$$

where in this equation, A_{Fe} , A_{ring} , and R_{ring} are calculated as follows:

$$A_{Fe} = 2(A_{Fe,1} + A_{Fe,2} + A_{Fe,3} + A_{Fe,4}) \quad (30)$$

$$A_{ring} = A_{Fe,1} \quad (31)$$

$$R_{ring} = \frac{r_{out} + r_{eq,i}}{2}. \quad (32)$$

The average tangential stress in the equivalent ring can be represented as follows:

$$\sigma_{tan,ave} = R_{ring}^2 \omega^2 \rho_{eq} \quad (33)$$

where ω is the angular velocity of the rotor.

Two dimensionless factors are applied to the calculated stress to ascertain the maximum stress, the safety factor, and the stress concentration factor.

$$\sigma_{max} = K_{safe} K_{scf} \sigma_{cir} \quad (34)$$

where the K_{safe} is the safety factor and K_{scf} is the stress concentration factor. It is common practice to incorporate a safety factor within the range of 1.5 to 2 to assure the safe operation of the machine under any uncertainties or variations in operating conditions.

The stress concentration factor quantifies the concentration of stress in the corners of flux barriers. This factor is heavily influenced by the geometry of the flux barrier, particularly the regions adjacent to the bridges and the fillet radius. This factor can be obtained using some reference models as presented in paper [34] or by performing FEM simulations. Some analytical models are available in the literature however they are for specific barrier shapes and may not encompass all possible scenarios.

B. FEM-AIDED MECHANICAL STRESS CALCULATION METHOD

In this study, an FEA-aided approach has been adopted to evaluate the mechanical stress values on the tangential and central bridges of the rotor. Initially, the analytical model discussed in the Section III-A was employed to predict the stress within the rotor structure, serving as the foundation for the initial calculations. To validate and refine these predictions, a series of FEM simulations were conducted across a variety of design configurations, including different numbers of poles, rotor diameters, and rotor geometries.

Discrepancies were identified, and correction coefficients were calculated by comparing the stress values obtained from the analytical model and the FEM simulations. These coefficients were then used to adjust the outputs of the analytical model, reducing the error margin and increasing the reliability of the predictions.

To quantify the degree of stress concentration, the ratio between the maximum stress obtained from the FEM simulations and the maximum stress derived from the analytical method was computed. This ratio, known as the “*stress concentration factor*” serves as a measure of the stress concentration phenomenon in the analyzed structure. An extensive look-up table was developed through an iterative process of analysis, comparison, and adjustment for a wide range of design configurations. This table integrates the correction coefficients corresponding to various design parameters, significantly enhancing the accuracy of mechanical stress calculations within the sizing tool.

Despite these efforts, some degree of error may persist in the stress calculations for certain specific design configurations. However, given the preliminary nature of the sizing process, it is believed that these errors fall within an acceptable range. The look-up table for stress concentration factors, created from this process, serves as a valuable resource for design purposes, aiding engineers in selecting appropriate stress concentration factors based on the specific geometry of the rotor under consideration.

IV. ELECTROMAGNETIC MODELING OF THE IPM MACHINE

The electromagnetic model of IPM machines developed in this section takes advantage of the magnetic equivalent network for estimating the performance in both no-load and load conditions, including the effects of saturation and material nonlinearities.

A. MAGNETIC EQUIVALENT NETWORK

Magnetic equivalent circuit is a simple and fast approach, which models the machine with several magnetic reluctances, and can predict the flux distribution in different parts of the machine. The more reluctance is considered, the more accurate field prediction is obtained.

A simple preliminary magnetostatic 2D-FEM simulation was performed to observe the flux distribution in different parts of rotor, aiming to build an associated magnetic equivalent network. In order to simplify the model as much as possible, the stator teeth were not considered, building a stator geometry resembling a slot-less IPM machine. The flux lines calculated by FEM at no-load condition are shown in Fig. 4.

It can be clearly seen that the flux generated by the magnets can be divided into two main paths. The first one indicates the flux path through the magnet, while the second one represents the leakage flux through the tangential and central iron bridges.

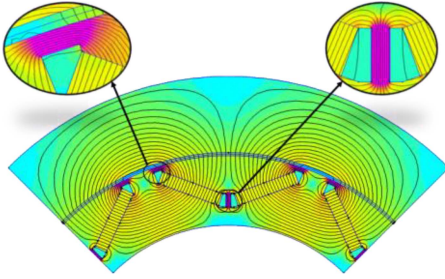


FIGURE 4. Representation of flux lines in a V-shape IPM machine.

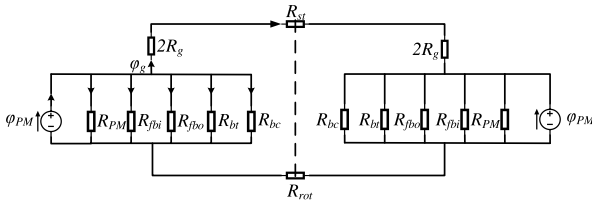


FIGURE 5. Magnetic network of the IPM machine.

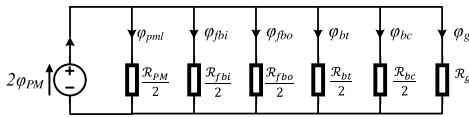


FIGURE 6. Simplified magnetic circuit of IPM machine.

However, under deep saturation, minor flux leakage may occur within the flux barriers, although this is typically negligible during the initial sizing phase.

Taking into account the flux paths previously described, the magnetic circuit can be primarily characterized by the magnets, the air gap adjacent to one pole pitch, the tangential and central iron bridges, the stator's back iron, and the rotor pole, as illustrated in Fig. 5.

The stator back iron and rotor yoke are not saturated since the relative permeability of the iron $\mu_{r,Fe}$ is very high. As a result, the value of these two reluctances (reluctance of stator back iron R_{St} and reluctance of rotor pole R_{rot}) and consequently their resultant magnetomotive force (MMF) drops are very small. Hence, they can be neglected to speed up the calculation process. Hence, they can be neglected to speed up the calculation process. So, the magnetic circuit shown in Fig. 5 can be simplified in a straightforward form, as shown in Fig. 6. In this magnetic circuit, φ_g and R_g denote the value of magnetic flux density in the air gap over the rotor pole and air gap reluctance, respectively.

The reluctance of the flux barriers can be divided into three parts, the reluctances due to the innermost and outermost extension of flux barriers (R_{fbi} and R_{fbo}), and the reluctance of permanent magnet R_{PM} . It should be noted that these three reluctances are interconnected in parallel to align with the flux trajectory within the machine. φ_{bc} and φ_{bt} are corresponding

magnet flux leakage in the bridges. This leakage contributes to significant saturation within central and tangential bridges, exacerbated by their relatively small cross-sectional areas. Consequently, the reluctance of central bridge R_{bc} and the reluctance of tangential bridge R_{bt} , are influenced by the magnetic flux density. This is due to their composition from magnetically nonlinear materials, which tend to operate under conditions ranging from moderate to high saturation. The main objective now is to solve the magnetic circuit compute the air gap magnetic flux φ_g .

Solving a magnetic equivalent network with nonlinear reluctances typically involves iterative methods and numerical calculations. Therefore, minimizing nonlinear reluctances, particularly in early design stages, is advantageous. Precise determination of the reluctance in each region is essential for the accuracy of the magnetic equivalent circuit's representation. Subsequently, by applying Kirchhoff's voltage and current laws, the circuit can be solved, allowing for the straightforward calculation of the magnetic flux and magnetic potential for each nose and branch, respectively.

The generated flux by one magnet and its corresponding reluctance can be calculated by the following:

$$\varphi_{pm} = K_{fill,pm} B_r l_{st} l_{PM} = B_r l_{st} l_{PM,eff} \quad (35)$$

$$\mathcal{R}_{PM} = \frac{h_{pm}}{K_{fill,pm} \mu_0 \mu_{PM} l_{st} l_{PM}} = \frac{h_{pm}}{\mu_0 \mu_{PM} l_{st} l_{PM,eff}} \quad (36)$$

where B_r is the residual magnetic flux density, μ_0 is the permeability of the air, and μ_{PM} is the relative recoil permeability of magnets. For conventional magnets, the recoil permeability of magnets μ_{PM} is usually close to one.

It should be remarked that when the magnet fill factor is less than one, two small areas will be added to the flux barriers. The reluctance of each section is determined by the following:

$$\mathcal{R}_{PMg} = \frac{h_{pm}}{\mu_0 l_{st} l_{pm} (1 - K_{fill,pm})}. \quad (37)$$

The geometry of the outer flux barrier can be approximated as a trapezoidal shape, and the reluctance of this region can be calculated as follows:

$$\mathcal{R}_{fbo} = \frac{h_{fbo}}{\mu_0 l_{st} (W_{fbo2} - W_{fbo1})} \ln \left(\frac{W_{fbo2}}{W_{fbo1}} \right). \quad (38)$$

The reluctance of the inner flux barrier can be modelled by two separate reluctances connected in parallel. The first part corresponds to the tangential extension of the flux barrier, which has a rectangular shape, and the second part is the triangular shape of the inner barrier.

The reluctance of the air gap facing one pole R_{airgap} can be calculated by the following:

$$\mathcal{R}_{airgap} = \frac{r_{out} + \frac{g}{2}}{\mu_0} \ln \left(1 + \frac{g_{eff}}{r_{out} + \frac{g}{2}} \right) \quad (39)$$

where g_{eff} is the effective length of the air gap considering the effects of stator slots by means of Carter's factor

$$g_{\text{eff}} = gK_{\text{carter}} \quad (40)$$

$$K_{\text{carter}} = \frac{\tau_{\text{slot},t}}{\tau_{\text{slot},t} - W_{\text{so,eq}}} \quad (41)$$

$$W_{\text{so,eq}} = \frac{2}{\pi} \left(\tan \left(\frac{W_{\text{so}}}{2g} \right) - \frac{2g}{W_{\text{so}}} \ln \left(1 + \left(\frac{W_{\text{so}}}{2g} \right)^2 \right) \right) \quad (42)$$

where $W_{\text{so,eq}}$ is the equivalent slot opening in which the flux density is zero [22].

The thickness of central and tangential bridges is constant. Therefore, the reluctance of central and tangential bridge is determined by the following:

$$\mathcal{R}_{bc} = \frac{h_{bx}}{\mu_0 \mu_{fe,bc} l_{st} \frac{w_{bi}}{2}} \quad (43)$$

$$\mathcal{R}_{bt} = \frac{h_{bt}}{\mu_0 \mu_{fe,bt} l_{st} w_{bo}} \quad (44)$$

$$h_{bt} = \left(r_{\text{out}} + \frac{W_{bo}}{2} \right) (\pi \gamma) \quad (45)$$

where h_{bt} is the equivalent width of the tangential bridge, $\mu_{fe,bc}$ and $\mu_{fe,bt}$ are the relative recoil permeability of the iron in the central and tangential bridges, respectively.

According to Kirchhoff's MMF law, the total MMF drops in a closed-loop circuit is equal to the total of the MMF sources.

For the simplified equivalent circuit shown in Fig. 6, the MMF of the rotor due to the magnets $F_{r,\text{pm}}$ can be calculated by the following:

$$F_{r,\text{pm}} = 2\varphi_{\text{pm}} \mathcal{R}_{\text{eq}} \quad (46)$$

$$2\varphi_{\text{pm}} = \varphi_{\text{pm},l} + \varphi_{fbi} + \varphi_{fbo} + \varphi_{bc} + \varphi_{bt} + \varphi_g \quad (47)$$

where \mathcal{R}_{eq} is the equivalent reluctance seen from the source or magnet, and it can be determined by the following:

$$\mathcal{R}_{\text{eq}} = \frac{1}{\frac{2}{\mathcal{R}_{\text{PM}}} + \frac{2}{\mathcal{R}_{fbi}} + \frac{2}{\mathcal{R}_{fbo}} + \frac{2}{\mathcal{R}_{bc}} + \frac{2}{\mathcal{R}_{bt}} + \frac{1}{\mathcal{R}_g}} \quad (48)$$

It should be noted that all the methodologies taken into account for reducing the resistive network, including series/parallel combination and voltage/current division, can be applied to lumped parameters magnetic circuit.

Finally, the air gap flux density can be calculated as follows:

$$B_g = \frac{\varphi_g}{A_g} \quad (49)$$

$$A_g = \tau_{\text{pole}} L_{st} \quad (50)$$

where A_g is the cross-sectional area of pole pitch.

The air gap flux density distribution in PM machines can be approximated by a square or trapezoidal shape [35], [36], [37]. Generally, the trapezoidal waveform is usually considered to analytically calculate the air gap flux density in the IPM machine, as depicted in Fig. 7.

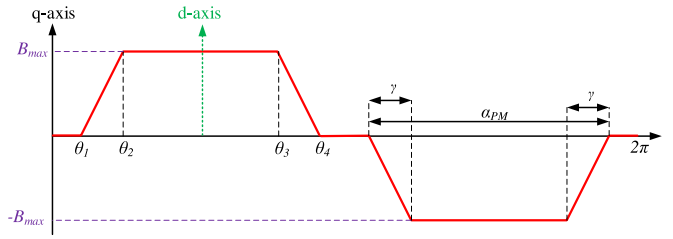


FIGURE 7. Equivalent distribution of air gap flux density in no-load conditions.

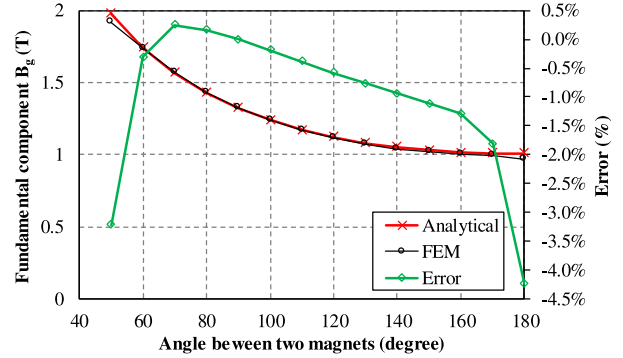


FIGURE 8. Comparison of the first harmonic of air gap flux density versus the β angle.

The shape of the trapezoidal function depends on magnetic polar pitch α_{PM} and barrier angle γ . According to the geometric parameter of the machine presented in Fig. 2, the trapezoidal function can be yielded

$$B_g(\theta_m) = \begin{cases} 0, & 0 \leq \theta_m \leq \theta_1 \\ \frac{B_{\text{max}}}{\theta_2 - \theta_1} (-1)^{\theta_m}, & \theta_1 \leq \theta_m \leq \theta_2 \\ B_{\text{max}} (-1)^{\theta_m}, & \theta_2 \leq \theta_m \leq \theta_3 \\ \frac{-B_{\text{max}}}{\theta_4 - \theta_3} (-1)^{\theta_m}, & \theta_3 \leq \theta_m \leq \theta_4 \\ 0, & \theta_4 \leq \theta_m \leq \frac{\pi}{P} + \theta_1 \end{cases} \quad (51)$$

To validate the analytical procedure, several IPM machines have been modelled, keeping fixed the outer radius of the rotor ($r_{\text{out}} = 150$ mm) and changing the angle between magnets from the minimum possible to 180° .

It should be remarked that the length of the magnets in this analysis varies with respect to the β angle. Fig. 8 compares the fundamental harmonic amplitudes of the waveforms computed analytically and by FEM. As seen, there is a good matching between the results, in particular for practical values of the β angle.

B. STATOR MMF

The winding diagram and winding function waveform of phase A for a two-pole machine are depicted in Fig. 9, where θ_r is the angular position in the stator reference frame, and N_{ph} denotes the number of turns in series per phase.

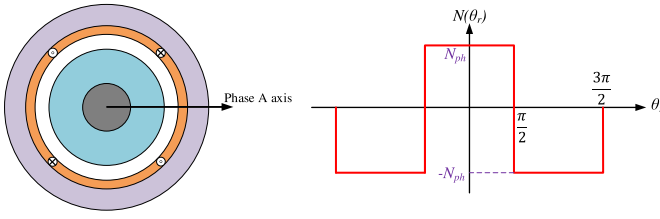


FIGURE 9. Winding function of phase A.

Generally, the Fourier form of winding function for phase A can be written as follows:

$$N(\theta_r) = \sum_{h=1, 2, 3, \dots}^{\infty} (-1)^{(k-1)} \frac{2N_{ph}K_{w,2h-1}}{\pi P} \frac{\cos((2h-1)(\theta_r))}{(2h-1)} \quad (52)$$

where h is the harmonic order and $K_{w,h}$ is the h th harmonic of winding factor.

The injected current in the winding for an m -phase machine can be given as follows:

$$I_{a, b, c, \dots} = I_{\max} \cos\left(\omega t - \frac{(j-1)\pi}{m} + \varphi\right), \quad j = 1, 2, \dots, m \quad (53)$$

where I_{\max} is the magnitude of current per phase, ω is the electrical angular frequency, and φ is the angle of phase current with respect to the d -axis, and j denotes the index of each phase.

For a three-phase machine, the stator MMF generated by the distributed stator winding can be written by the currents is obtained by the following:

$$F_{st}(\theta_r, t) = N_a I_a + N_b I_b + N_c I_c \quad (54)$$

$$\begin{cases} N_a = \sum_{k=1, 2, 3, \dots}^h (-1)^{(k-1)} \frac{2N_{ph}K_{w,2h-1}}{\pi P} \frac{\cos((2k-1)\theta_r)}{2k-1} \\ N_b = \sum_{k=1, 2, 3, \dots}^h (-1)^{(k-1)} \frac{2N_{ph}K_{w,2h-1}}{\pi P} \frac{\cos((2k-1)(\theta_r - \frac{2\pi}{3}))}{2k-1} \\ N_c = \sum_{k=1, 2, 3, \dots}^h (-1)^{(k-1)} \frac{2N_{ph}K_{w,2h-1}}{\pi P} \frac{\cos((2k-1)(\theta_r - \frac{4\pi}{3}))}{2k-1} \end{cases} \quad (55)$$

$$F_{st}(\theta_r, t) = \sum_{k=1, 2, 3, \dots}^h F_{st, \max, 2h-1} \cos\left\{ (2k-1) \left(\theta_r + (-1)^{(k-1)} (\omega t + \varphi) \right) \right\} \quad (56)$$

$$F_{st, \max, h} = 3 \frac{N_{ph}K_{w,h}}{Ph\pi} I_{\max} \quad (57)$$

To simplify the analysis, it is possible to decompose the stator current into d -axis and q -axis components. Therefore, the MMF of the stator can be divided into the d -axis and q -axis components. This also allows to approach the design

and analysis of the machine in a more pragmatic manner

$$F_{st}(\theta_r, t) = \overbrace{F_{st,d}(\theta_r, t)}^{d\text{-axis MMF}} + \overbrace{F_{st,q}(\theta_r, t)}^{q\text{-axis MMF}} \quad (58)$$

C. ROTOR MMF

Rotor MMF composes of two components, rotor MMF generated by magnets $F_{r,PM}$ and rotor MMF produced by the magnetic potential of the stator $F_{r,a}$

$$F_r = F_{r,PM} + F_{r,a} \quad (59)$$

The rotor MMF created by magnets is related to the air gap flux density and it can be expressed as follows:

$$F_{r,PMh} = \mathcal{R}_g \varphi_{g,h} = \frac{\mu_0}{g} B_{g,h} \quad (60)$$

Note that applying the MMFs superposition (59), the airgap flux density waveform at load condition can be computed, assuming negligible the rotor pole and stator core saturation in presence of slot currents.

The approximately infinite permeance region above the magnetic barriers results in an equipotential area on the top surface of the flux barrier. The magnetic voltage drop across the magnetic barrier is represented by the waveforms of the rotor MMF created by the stator MMF [38], [39]. In this circumstance, the magnets are deactivated, and only the impact of the flux barriers on the rotor MMF is taken into account. A similar magnetic circuit represented in Fig. 6 can be employed to calculate the $F_{r,a}$ replacing the magnets with air. By solving the magnetic circuit under this condition, the value of $F_{r,a}$ can be computed by the following:

$$F_{r,a} = \sum_{h=1,3,5,\dots}^{\infty} F_{r,a_h} \cos((h \pm 1)\omega t \mp \psi) \quad (61)$$

where ω is the angular position of rotor, and ψ is the current angle.

D. ELECTROMAGNETIC TORQUE CALCULATION

The electromagnetic torque may be computed by means of the Lorentz force law along the air gap surface, and it can be expressed as follows [39], [40], [41], [42]:

$$\begin{aligned} T_{ele} &= \left(r_{out} + \frac{g}{2} \right) L_{st} \int_0^{2\pi P} B_{airgap} dF_{st} \\ &= P \frac{\mu_0}{g} \left(r_{out} + \frac{g}{2} \right) L_{st} \left[\int_0^{2\pi} F_r \frac{dF_{st}}{d\theta} d\theta - \int_0^{2\pi} F_{st} \frac{dF_r}{d\theta} d\theta \right] \end{aligned} \quad (62)$$

Considering the periodicity of the stator MMF, the second part of this integral is equal to zero. So, the electromagnetic torque equation can be written as follows:

$$T_{ele} = P \frac{\mu_0}{g} \left(r_{out} + \frac{g}{2} \right) L_{st} \int_0^{2\pi} F_r \frac{dF_{st}}{d\theta} d\theta \quad (63)$$

Substituting Fourier forms of the stator and rotor MMF into electromagnetic torque equation, it is possible to compute both average torque component resulting from the fundamental component and torque ripple due to the harmonic components

$$T_{ave} = \pi F_{st,1} F_{r,1} \sin(\psi) \quad (64)$$

$$T_{ripple} = \sum_{\substack{h=6m \pm 1 \\ m=1,2,3, \dots}}^{\infty} [h F_{st,h} F_{r,h} \sin((h \pm 1)\omega t \mp \psi)] \quad (65)$$

$$T_{ele} = T_{ave} + T_{ripple}. \quad (66)$$

E. STATOR LAMINATION GEOMETRY

Neglecting the leakage, the maximum flux in the stator back-iron is half of the flux generated in each pole. Therefore, the thickness of the stator back-iron can be calculated as follows:

$$\frac{\varphi_{pole}}{2} = K_{fe} B_{cs,max} L_{cs} L_{st} \quad (67)$$

$$L_{cs} = \frac{B_{g,fund}}{2PK_{fe}B_{cs}L_{st}} \pi \alpha_{PM} r_{s,i} \quad (68)$$

where φ_{PM} is the generated flux density in each pole, K_{fe} is the stacking factor, $B_{g,fund}$ is the fundamental component of air-gap flux density, B_{cs} is the maximum permissible flux density in the stator back-iron, and L_{st} is the axial length of the machine.

The slot dimensions can be obtained on the basis of the required cross-section of conductive materials or copper A_{Cu} that is chosen to satisfy the cooling specifications. However, to have more accurate slot geometry, this area should be adjusted with respect to the conductor's shapes, insulation thickness (e.g., slot liner), and winding arrangement. For this purpose, slot fill factor $K_{Cu,fill}$ is considered to have a more realistic slot geometry. The useful area of the slot can be calculated as follows:

$$A_{us} = \frac{A_{Cu}}{K_{Cu,fill}}. \quad (69)$$

It should be highlighted that high slot fill factor results in reducing the resistance, copper Joule loss, thermal resistance, and temperature rise. The highest slot fill factor can be around 0.4–0.5 for the coils with random wound conductors. However, it can be as high as 0.8 by means of uninsulated and rectangular conductors or hairpin winding [24], [43].

The maximum value of flux density in the stator tooth B_{ts} is considered a design constraint during the sizing procedure. This value can be validated in the tooth section. Neglecting the leakage, the width of the stator teeth can be calculated by taking into account the flux density over a slot pitch as follows:

$$W_{tt} = \frac{B_{g,fund}}{K_{fe}B_{ts}} \tau_{slot} \quad (70)$$

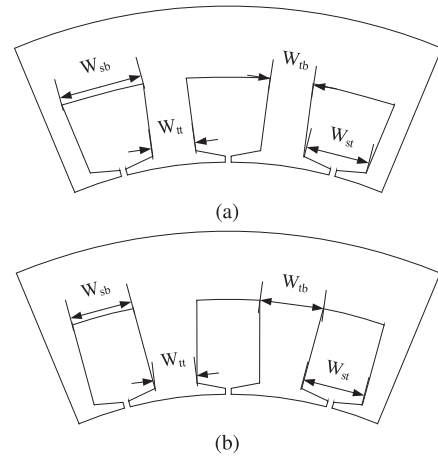


FIGURE 10. Conventional slot shape. (a) Trapezoidal slot. (b) Rectangular slot.

where the slot pitch τ_{slot} at the inner radius of the stator can be calculated by the following:

$$\tau_{slot} = \frac{2\pi r_{s,i}}{Q}. \quad (71)$$

Subsequently, the top width of the stator slot can be calculated as follows:

$$W_{st} = \frac{2\pi r_{s,i}}{Q} - W_{tt}. \quad (72)$$

However, the thickness of slot enclosure h_r should be considered for the calculation of slot geometry in case of semi-closed slot shape. So, the stator slot width is evaluated at the radius r_h

$$h_r = h_{ls} + h_{es} \quad (73)$$

$$r_h = r_{s,in} + h_r \quad (74)$$

where h_{ls} and h_{es} are the stator tooth tips as shown in Fig. 1. If the stator tooth tips are very thin or tapered, they are liable to saturate and increase the slot opening, leading to increasing the slot ripple and consequently cogging and rotor eddy-current loss.

Generally, the stator slot can have a trapezoidal shape, so-called parallel tooth, in which the width of the stator teeth is constant along the radial direction as shown in Fig. 10(a), or they can have a rectangular shape, so-called parallel slot, in which width of the stator teeth increase over the radius as shown in Fig. 10(b).

For the trapezoidal slot shape, since the width of the stator tooth is constant, the bottom width of the slot can be computed using the following equations:

$$W_{tt} = W_{tb} \quad (75)$$

$$W_{sb} = W_{st} + \frac{2\pi h_{us}}{Q} \quad (76)$$

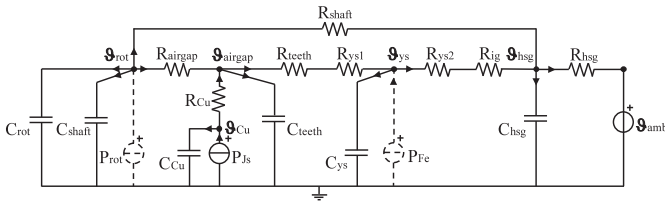


FIGURE 11. Conventional lumped-parameters thermal network for the temperature prediction of different parts of an electrical machine.

$$h_{us} = \frac{-\frac{QW_{st}}{\pi} + \sqrt{\left(\frac{QW_{st}}{\pi}\right)^2 + \frac{4Q}{\pi}A_{us}}}{2}. \quad (77)$$

Knowing the useful area of slot A_{us} and the top width of the stator slot W_{st} , the useful height of the slot for the rectangular shape can be computed by the following:

$$h_{us} = \frac{2A_{us}}{(W_{st} + W_{sb})}. \quad (78)$$

Obviously, the bottom width of stator slot W_{sb} is equal to the top part in case.

The total height of slot h_{ts} and total area of slot A_{ts} can be respectively calculated by the following:

$$h_{ts} = h_{us} + h_{es} + h_{ls} = h_{us} + h_r \quad (79)$$

$$A_{ts} = A_{us} + W_{so}h_{es} + \frac{W_{so} + W_{st}}{2}h_{ls}. \quad (80)$$

In addition, the dimensions of the stator tooth can be computed as follows:

$$W_{tt} = \frac{2\pi r_h}{Q} - W_{st} \quad (81)$$

$$W_{tb} = \frac{2\pi r_h}{Q} - W_{sb}. \quad (82)$$

Finally, the external radius of the stator can be calculated by taking into account the slot dimensions and the length of the stator back-iron.

Some fillets are applied during the manufacturing process for the sharp edges and corners (i.e., stator slots and rotor cavities). It should be pointed out that these manufacturing aspects are not taken into account during the design stage.

V. THERMAL MODELING

The simplified lumped parameters thermal network (LPTN) illustrated in Fig. 11 has been employed to perform a preliminary thermal assessment of the designed machine. Several thermal resistances and capacitances are considered in this thermal network to predict the temperature accurately. In this model, the thermal resistances and capacitances are calculated based on the machine geometry of the designed machine. The calculation of thermal capacitance and resistances can be found in model [44], [45], [46].

Generally, the total value of losses on the rotor (including iron losses on the rotor core, magnet loss, and mechanical

loss), winding Joule losses, and iron losses on the stator core are taken into consideration for the thermal analysis. It is worth noting that the designer should set the mechanical loss during the sizing procedure as the percentage of the rated power of the machine. The temperature in the different nodes of the thermal network can be computed by solving the differential equations:

$$\frac{d\vartheta_{rotor}}{dt} = \frac{P_{rotor}}{C_{rotor}} + \frac{\vartheta_{airgap} - \vartheta_{rotor}}{C_{rotor}R_{airgap}} + \frac{\vartheta_a - \vartheta_{rotor}}{C_{rotor}R_{R,fix}} \quad (83)$$

$$\frac{d\vartheta_{cu}}{dt} = \frac{P_{js}}{C_{cu}} + \frac{\vartheta_{airgap} - \vartheta_{cu}}{C_{cu}R_{cu}} \quad (84)$$

$$\begin{aligned} \frac{d\vartheta_{airgap}}{dt} &= \frac{\vartheta_{ys} - \vartheta_{airgap}}{C_{teeth}(R_{teeth} + R_{ys1})} + \frac{\vartheta_{cu} - \vartheta_{rotor}}{C_{teeth}R_{cu}} \\ &+ \frac{\vartheta_{rotor} - \vartheta_{airgap}}{C_{teeth}R_{airgap}} \end{aligned} \quad (85)$$

$$\frac{d\vartheta_{ys}}{dt} = \frac{P_{Fe}}{C_{ys}} + \frac{\vartheta_{airgap} - \vartheta_{ys}}{C_{ys}(R_{teeth} + R_{ys1})} + \frac{\vartheta_{s,fix} - \vartheta_{ys}}{C_{ys}(R_{ys2} + R_{ig})} \quad (86)$$

$$\frac{d\vartheta_{s,fix}}{dt} = \frac{\vartheta_{ys} - \vartheta_{s,fix}}{C_{s,fix}(R_{ys2} + R_{ig})} + \frac{\vartheta_a - \vartheta_{s,fix}}{C_{s,fix}R_{s,fix}} \quad (87)$$

where in the above equations, the parameters are defined as follows:

- ϑ_{rotor} is the temperature of the rotor;
- ϑ_{airgap} is the temperature at the machine air gap;
- ϑ_{cu} is the winding temperature;
- ϑ_{ys} is the stator yoke temperature;
- $\vartheta_{s,fix}$ is the stator fixture temperature;
- ϑ_a is the ambient temperature;
- C_{rot} is the thermal capacitance of the rotor yoke and magnets;
- $C_{R,fix}$ is the thermal capacitance of the rotor fixture;
- $R_{R,fix}$ is the thermal resistance of the rotor fixture;
- R_{airgap} is the thermal resistance of air gap;
- R_{cu} is the thermal resistance between the stator winding and stator core;
- R_{hsg} is the thermal resistance of housing;
- R_{teeth} is the thermal resistance of stator teeth;
- C_{hsg} is the thermal capacitance of housing;
- C_{cu} is the thermal capacitance of the stator winding;
- C_{teeth} is the thermal capacitance of the stator teeth;
- R_{ys1} is the thermal resistance of the inner yoke;
- R_{ys2} is the thermal resistance of outer stator yoke;
- C_{ys} is the thermal capacitance of the stator yoke;
- R_{ig} is the thermal resistance of the interface airgap between the stator core and its fixture.

VI. GEOMETRICAL DESIGN PROCEDURE OF IPM MACHINE

In the geometrical design methodology, the rotor geometry is incrementally scaled up step by step to achieve the desired torque value while maintaining the magnet thickness constant.

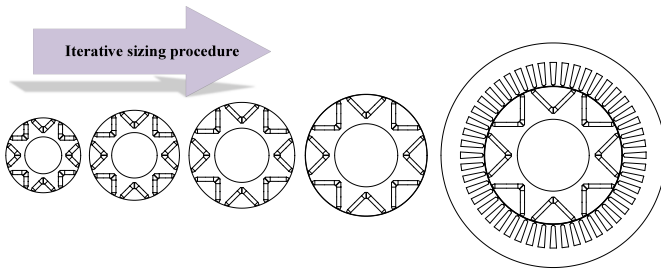


FIGURE 12. Iterative design procedure.

A similar procedure has been applied to design induction machines and inner or outer surface-mounted PM machines [47]. This approach allows for computing the machine specification very fast and with reasonable accuracy, thanks to MEC in this specific case.

The iterative design technique involves three initial input categories as follows.

- 1) Rated specifications: Base torque, base speed, maximum speed, terminal voltage, and number of poles.
- 2) Winding specification: Winding type (single or double layer), reduced pitch (defined as the number of stator slots), and the number of stator slots.
- 3) Design constrains: Electromagnetic and mechanical properties of soft and hard materials, thickness of magnets h_{PM} , air gap length, the ratio of the axial length of the machine over air gap diameter (aspect ratio) λ , magnet polar pitch α_{PM} , the angle between two magnets β , slot opening W_{so} , stator current density J_s , and maximum value of the stator electrical loadability $A \times J_s$.

The initial step in the geometrical design procedure involves constructing the rotor geometry. To ensure a feasible geometry, the following conditions are imposed.

- 1) The minimum length of the magnet $l_{pm,min}$ should be equal to or larger than the magnet thickness h_{pm} ($l_{pm,min} \geq h_{pm}$).
- 2) The calculated inner diameter of the rotor should be equal or larger than the minimum inner diameter of the rotor ($D_{r,in} \geq D_{r,in,min}$).
- 3) The minimum slot pitch should be equal to or twice time larger than the slot opening, $\tau_{slot} \geq 2W_{so}$.

After establishing the basic parameters that identify the layout of the rotor, the air gap diameter is gradually increased, as shown in Fig. 12 up to the time the imposed constraints are satisfied, and the torque performance is reached.

The thicknesses of the tangential and central bridges are evaluated from the structural point of view at each step based on the yield strength of the materials. It is important to note that the designer should initially specify a minimum thickness for the tangential and central bridges. However, these values will be reevaluated during the design process. This decision is made to account for manufacturing constraints and expedite the calculation process. In practice, achieving bridge thicknesses less than a fraction of a millimeter can be challenging. As explained earlier, the stress concentration and safety

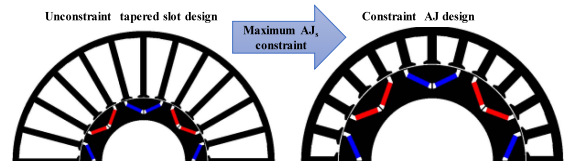


FIGURE 13. Tapered slot design.

factors should be applied to guarantee the safe operation of the rotor. The safety factor ($1 < K_{safe} \leq 2$) can be imposed by the designer, while the stress concentration factor is obtained by means of a FEA-aided method. This approach can minimize the computational time and improve the design process of the machine. It is worth highlighting that the fillet factor is kept constant to $r_{fillet} = 0.2$ mm for mechanical stress calculation. Increasing the fillet factor on the barrier's edges can reduce the stress value in these areas.

Knowing the machine geometry makes it possible to derive an equivalent magnetic circuit to calculate the rotor MMFs as explained in detail in Section IV-C.

During the sizing procedure, it is usually assumed that the permeability of the stator teeth and yoke are infinite, and there is no MMF drop in these regions. However, in actual operating conditions the stator region experiences nonnegligible saturation, especially in the stator teeth. This saturation results in a considerable portion of the air gap magnetic flux passing through the slot air rather than going through the stator teeth. Consequently, this issue leads to an underestimation of the necessary MMF required to obtain the desired output torque. This MMF drop can be calculated by means of a recursive procedure as reported in detail in papers [48], [49]. This MMF drop can be incorporated into the stator MMF in each step to enhance the accuracy of the electromagnetic design.

The exit condition of the proposed design procedure is an important step in obtaining an appropriate electromagnetic design. Although, for any values of the outer diameter of the rotor satisfying the torque constraint, the stator lamination design routine provides a slot geometry, for small air gap diameter may converge to a solution in which the outer diameter of the stator is relatively large, and the slot shape might not be feasible as shown in Fig. 13

To avoid this condition and acquire a proper design, the maximum product of the linear current density A and the current density J_s , that is, the stator electrical loadability of the machine, was defined as an input parameter in the proposed approach.

It is worth noting that $A \times J_s$ product is directly related to the thermal dissipation of the generated loss in the winding and rotor diameter, and it should be chosen carefully considering the thermal management system. However, some margin should be conveniently kept considering that other loss components are active in the machine, namely the iron losses, particularly on the stator. In literature, graphs showing the A trends function of the rotor diameter and the values of J_s and $A \times J_s$ are available. The selection of the $A \times J_s$ product is often based on the basis of the designers' experience.

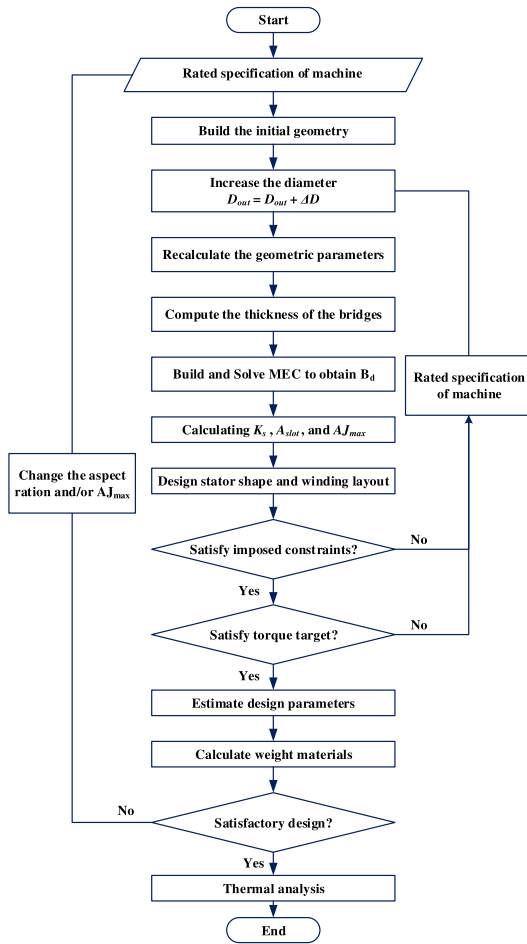


FIGURE 14. Flowchart of the iterative design process for IPM machines.

Finally, all the geometric and winding parameters are computed. Apart from the geometric parameters, the design tool can also compute the weight, losses, equivalent circuit parameters, and temperature of different parts of the machine. The designer can choose the step size of the iterative design. Once basic choices about the expected machine dimensions are made. This can significantly reduce the computational time during the design procedure. Fig. 14 represents the design process flowchart for the V-shaped IPM machine, which is based on a progressive increase in rotor diameter.

It is worth mentioning that the designer has the flexibility to set the step size for the iterative design process. By carefully selecting the step size, the designer can substantially accelerate the design and analysis phases, making the process more efficient and less time-consuming.

In the proposed sizing approach, the design not only meets torque requirements but also aligns with efficient control strategies by incorporating an analysis of the maximum torque per ampere (MTPA) control mode. This aspect involves evaluating the optimal current phase angle for maximizing torque by systematically varying the current angle from 0° to 90° and computing the resultant torque for each angle. This thorough examination ensures that the design can operate at peak

TABLE I Input Parameters Kept Fixed for the Two Designed Models

Parameter	Value
Rated fundamental phase voltage	400 V
Stator current density	6 A/mm ²
Slot fill factor	0.4
Slot/pole/phase	2
Maximum teeth flux density	1.2 T
Maximum stator yoke flux density	1 T
Lamination materials	M400-50A ^o
Magnet type	NdFeB 30HST

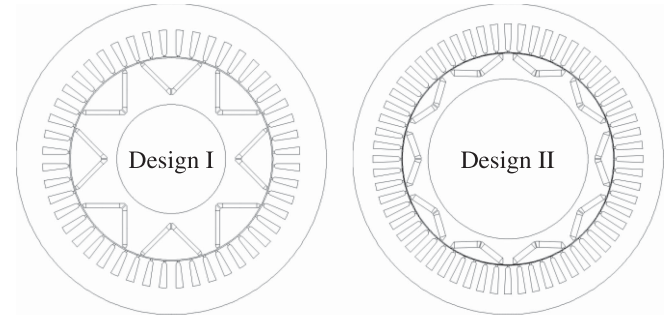


FIGURE 15. Schematic of two design models.

efficiency by utilizing the best possible current phase angle for torque production.

By integrating this MTPA control analysis into the iteration process, the design methodology considers the interaction between design parameters and control strategies. This integration is crucial for developing a machine that performs optimally under practical operating conditions.

It is important to note that including MTPA control analysis increases computational time due to the additional calculations required to identify the optimal current phase angle. However, this added complexity is justified by the valuable insights it provides, ultimately leading to a more robust and performance-optimized design.

VII. CASE STUDY

In order to validate the presented design procedure, two V-type IPM machines having different numbers of poles and rated torque have been designed. In detail, an 8-pole IPM motor with $\beta = 90^\circ$ called “Design I,” and one 10-pole IPM machine with $\beta = 140^\circ$ called “Design II,” were designed based on the proposed approach.

Some of the design input parameters have been kept fixed for the two machines, as reported in Table I. The main characteristics of the designed examples, including dimensions and the electrical parameters, are reported in Table II. Also, the schematic of the designed models is represented in Fig. 15.

The computations for this study were conducted on a computer equipped with an Intel Core i7-2670QM CPU @ 2.20 GHz, 16 GB RAM, running Windows 7. The computational times for the provided design examples, Design I and Design II, were 7.6 and 8.2 s, respectively. It is worth noting that

TABLE II Main Parameters of the Designed Machines

Parameter	Design I	Design II
Torque (Nm)	115	205
Base speed (rpm)	3000	1500
Max. speed (rpm)	9000	7500
Number of poles	8	10
α_{PM}	0.8	0.85
h_{PM} (mm)	4	6
β (deg)	90	140
Barrier angle γ	2.07	1.63
D_{er} (mm)	195	211
D_{es} (mm)	300.5	311.1
L_{st} (mm)	97.5	105.5
l_{pm} (mm)	34.7	23.9
$l_{pm,eff}$ (mm)	33.0	22.7
W_{bo} (mm)	1	0.8
W_{bi} (mm)	1.2	0.8
h_{ts} (mm)	25.9	28.4
w_{tooth} (mm)	9.0	6.7
L_{cs} (mm)	25.8	20.6
$A \times J_s$	1494	1994
I_{ph} (A _{rms})	40.7	48.1
Z_{ph}	131	184
A (A _{rms} /cm)	24900	33200
R_{ph} (Ω)	0.12	0.16

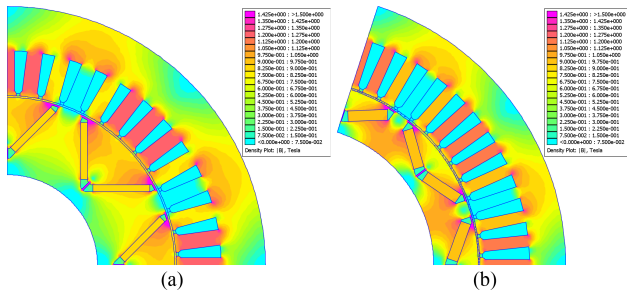


FIGURE 16. Distribution of magnetic flux density in the machine. (a) “Design I.” (b) “Design II.”

the inner diameter of the rotor for each design was set to zero. These results demonstrate the efficiency of the proposed sizing approach, highlighting its suitability for rapid preliminary design iterations.

A. FINITE-ELEMENT VALIDATION

As the first step of evaluation, the designed machines were modelled at no-load and load conditions by means of numerical 2D-FEM and their main parameters were calculated.

Fig. 16 shows the magnetic flux distribution of three designs at no-load conditions for “Design I” and “Design II.” The maximum permissible values of flux density in the stator yoke and stator teeth are in the range of input design parameters as reported in Table 1.

The two design models have been also assessed at load condition varying the phase of the vector current from zero degrees, where phase A is aligned with the q -axis at 90°,

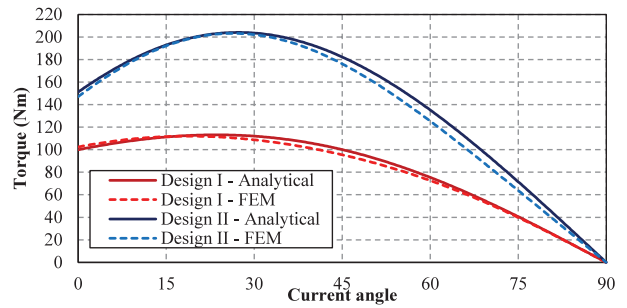


FIGURE 17. Comparison of torque–current angle characteristic curves of “Design I” and “Design II,” obtained by analytical procedure and FEM.

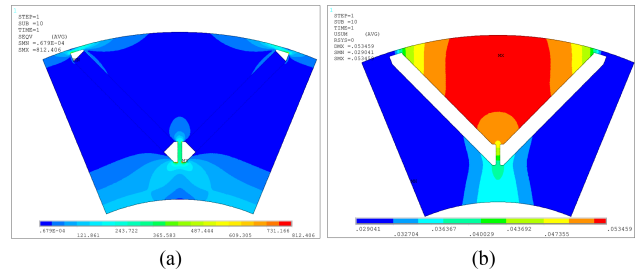


FIGURE 18. Distribution of mechanical stress in “Design I” at 9 k(r/min). (a) Von Mises stress. (b) Displacement.

where phase A is aligned with the d -axis, and torque were calculated.

Fig. 17 shows the output torque versus the current angle of the designed models as determined both through numerical FEM simulations. Clearly, the estimated torque aligns exceptionally well with the FEM results.

Upon comparing the outcomes presented in Fig. 16 with the specifications outlined in Table 2, it becomes apparent that the computational error for the designed models remains below 3%. This difference highlights the remarkable precision of the design process. However, it is important to state that this computational difference might slightly increase for extremely small and large values of β .

It is worth highlighting that the torque calculation is capable to compute both reluctance and PM torque components precisely. In addition, it offers the ability to swiftly determine the angle at which the maximum torque occurs.

Furthermore, the torque ripple of the machines is evaluated using both analytical and FEM methods, with a calculation error of around 6%. This calculation error can be reduced by considering higher harmonics during the calculation.

The machines have also been simulated in ANSYS Mechanical to assess structural integrity of the rotors and ascertain the maximum stress levels and displacements occurring within the rotor. Figs. 18 and 19 demonstrate the distribution of Von Mises stress and rotor displacement resulting from centrifugal forces within the rotor structure of “Design I” and “Design II,” respectively.

The computed maximum Von Mises within the machines are consistently below the yield stress of the lamination materials, remaining under 315 MPa. In detail, the maximum Von

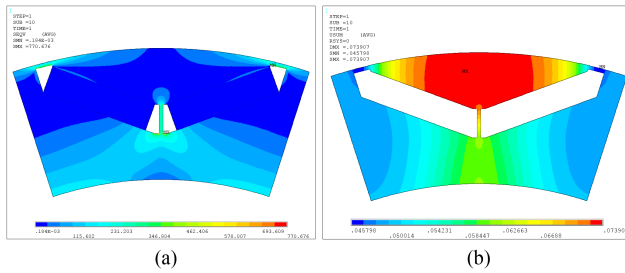


FIGURE 19. Distribution of mechanical stress in “Design II” at 10.5 k(r/min). (a) Von Mises stress. (b) Displacement.

TABLE III Temperature in Different Parts of the Machine Calculated Analytically and by Motor-CAD

Parameter	LPTN	ANSYS Motor-CAD
PM temperature	100.8°C	98.5°C
Winding temperature	128.9°C	125.9°C
Airgap temperature	111°C	109°C
Stator yoke temperature	113.6°C	112°C
Housing temperature	95.3°C	93.6°C

Mises stress are concentrated in the central bridges, where substantial centrifugal forces are at play. For Design II, the maximum stress reaches 298 MPa, while for Design I, it is 312 MPa.

The presented results can show the effectiveness of the proposed calculation methodology for the stress concentration factor. It should be mentioned that no safety factor was applied for the design examples. Applying a safety factor can maintain the possible discrepancies during the sizing stage.

It is worth emphasizing that the determination of the thickness for both central and bilateral bridges take into account the material properties and maximum rotational speed of the rotor. In practice, specific fillet radii are implemented along sharp edges, and certain bumps are usually placed near the corners of cavities to mitigate stress concentrations.

B. THERMAL EVALUATION

The steady-state temperatures across various machine parts were calculated using the presented LPTN and compared with a commercial software. Due to the dependency of thermal analysis on machine losses, material volumes, and their properties, only “Design I” was assessed to validate the thermal model. Table III presents a comparison of average temperatures values for critical machine parts (including magnets, winding, stator, and housing) calculated by the LPTN model and ANSYS Motor-CAD. Strong agreement is observed between the results.

VIII. CONCLUSION

This article proposed a comprehensive multidomain sizing algorithm tailored for V-shape IPM machines. The methodology combines geometric design principles, magnetic equivalent circuit analysis, mechanical stress calculations, and torque estimation within a cohesive framework. A versatile geometric model, driven by mathematical equations, integrates with an efficient stress calculation algorithm, finetuned through FEM-based design of experiments. To validate the precision of the proposed sizing methodology, two examples of V-shaped IPM machines were sized and subjected to FEM assessment. The successful achievement of target torque and maximum mechanical stress values validates the accuracy of the proposed sizing algorithm, firmly establishing its effectiveness for the initial stages of IPM machine design.

REFERENCES

- [1] M. A. Rahman, “History of interior permanent magnet motors [History],” *IEEE Ind. Appl. Mag.*, vol. 19, no. 1, pp. 10–15, Jan./Feb. 2013, doi: [10.1109/MIAS.2012.2221996](https://doi.org/10.1109/MIAS.2012.2221996).
- [2] R. Yang, N. Schofield, and A. Emadi, “Comparative study between interior and surface permanent magnet traction machine designs,” in *Proc. IEEE Transp. Electrific. Conf. Expo.*, Jun. 2016, pp. 1–6, doi: [10.1109/TTEC.2016.7520249](https://doi.org/10.1109/TTEC.2016.7520249).
- [3] L. Zhu, S. Z. Jiang, Z. Q. Zhu, and C. C. Chan, “Analytical modeling of open-circuit air-gap field distributions in multisegment and multilayer interior permanent-magnet machines,” *IEEE Trans. Magn.*, vol. 45, no. 8, pp. 3121–3130, Aug. 2009, doi: [10.1109/TMAG.2009.2019841](https://doi.org/10.1109/TMAG.2009.2019841).
- [4] A. Wang, Y. Jia, and W. L. Soong, “Comparison of five topologies for an interior permanent-magnet machine for a hybrid electric vehicle,” *IEEE Trans. Magn.*, vol. 47, no. 10, pp. 3606–3609, Oct. 2011, doi: [10.1109/TMAG.2011.2157097](https://doi.org/10.1109/TMAG.2011.2157097).
- [5] C.-C. Hwang and Y. H. Cho, “Effects of leakage flux on magnetic fields of interior permanent magnet synchronous motors,” *IEEE Trans. Magn.*, vol. 37, no. 4, pp. 3021–3024, Jul. 2001, doi: [10.1109/20.947055](https://doi.org/10.1109/20.947055).
- [6] Z. Li, X. Huang, Z. Chen, L. Wu, Y. Shen, and T. Shi, “Electromagnetic analysis for interior permanent-magnet machine using hybrid subdomain model,” *IEEE Trans. Energy Convers.*, vol. 37, no. 2, pp. 1223–1232, Jun. 2022, doi: [10.1109/TEC.2021.3112813](https://doi.org/10.1109/TEC.2021.3112813).
- [7] P. Wu and Y. Sun, “A novel analytical model for on-load performance prediction of delta-type IPM motors based on rotor simplification,” *IEEE Trans. Ind. Electron.*, vol. 71, no. 7, pp. 6841–6851, Jul. 2024, doi: [10.1109/TIE.2023.3309943](https://doi.org/10.1109/TIE.2023.3309943).
- [8] M. M. Ghahfarokhi, V. Z. Faradonbeh, E. Amiri, S. M. M. Bafrouei, A. D. Aliabad, and S. T. Boroujeni, “Computationally efficient analytical model of interior permanent magnet machines considering stator slotting effects,” *IEEE Trans. Ind. Appl.*, vol. 58, no. 4, pp. 4587–4601, Jul./Aug. 2022, doi: [10.1109/TIA.2022.3170536](https://doi.org/10.1109/TIA.2022.3170536).
- [9] P. Akiki et al., “Multiphysics design of a V-shape IPM motor,” *IEEE Trans. Energy Convers.*, vol. 33, no. 3, pp. 1141–1153, Sep. 2018, doi: [10.1109/TEC.2018.2803072](https://doi.org/10.1109/TEC.2018.2803072).
- [10] R. Lin, S. D. Sudhoff, and V. C. do Nascimento, “A multi-physics design method for V-shape interior permanent-magnet machines based on multi-objective optimization,” *IEEE Trans. Energy Convers.*, vol. 35, no. 2, pp. 651–661, Jun. 2020, doi: [10.1109/TEC.2019.2958928](https://doi.org/10.1109/TEC.2019.2958928).
- [11] J. F. Gieras, *Permanent Magnet Motor Technology: Design and Applications*. Boca Raton, FL, USA: CRC Press, 2009.
- [12] B. D. Cullity and C. D. Graham, *Introduction to Magnetic Materials*. Hoboken, NJ, USA: Wiley, 2011.
- [13] M. A. Darmani, S. Vaschetto, and A. Cavagnino, “Multiphysics design and modeling of rotating electrical machines,” in *Proc. 47th Annu. Conf. IEEE Ind. Electron. Soc.*, Oct. 2021, pp. 1–6, doi: [10.1109/IECON48115.2021.9589145](https://doi.org/10.1109/IECON48115.2021.9589145).
- [14] M. Ahmadi Darmani, “Multiphysics design of interior permanent magnet machines and characterization of innovative hard magnetic material,” Ph.D. dissertation, Politecnico Di Torino, Turin, Italy, 2022. Accessed: Jul. 29, 2023. [Online]. Available: <https://iris.polito.it/handle/11583/2971120>

- [15] I. Kleilat, K. E. K. Benkara, G. Friedrich, S. Vivier, N. Moubayed, and R. Dib, "Comparison of two analytical methods for calculating the maximum mechanical stress in the rotor of high-speed-assisted synchronous reluctance machines," *IEEE Trans. Ind. Appl.*, vol. 57, no. 2, pp. 1344–1353, Mar./Apr. 2021, doi: [10.1109/TIA.2020.3040946](https://doi.org/10.1109/TIA.2020.3040946).
- [16] X. Jannot, J.-C. Vannier, C. Marchand, M. Gabsi, J. Saint-Michel, and D. Sadarnac, "Multiphysics modeling of a high-speed interior permanent-magnet synchronous machine for a multiobjective optimal design," *IEEE Trans. Energy Convers.*, vol. 26, no. 2, pp. 457–467, Jun. 2011, doi: [10.1109/TEC.2010.2090156](https://doi.org/10.1109/TEC.2010.2090156).
- [17] P. Akiki et al., "Nonlinear analytical model for a multi-V-shape IPM with concentrated winding," *IEEE Trans. Ind. Appl.*, vol. 54, no. 3, pp. 2165–2174, May/Jun. 2018, doi: [10.1109/TIA.2018.2799175](https://doi.org/10.1109/TIA.2018.2799175).
- [18] N. Bracikowski, M. Hecquet, P. Brochet, and S. V. Shirinskii, "Multiphysics modeling of a permanent magnet synchronous machine by using lumped models," *IEEE Trans. Ind. Electron.*, vol. 59, no. 6, pp. 2426–2437, Jun. 2012, doi: [10.1109/TIE.2011.2169640](https://doi.org/10.1109/TIE.2011.2169640).
- [19] N. Bracikowski, M. Hecquet, P. Brochet, and S. V. Shirinskii, "Multiphysics Modeling of a Permanent Magnet Synchronous Machine by Using Lumped Models," *IEEE Trans. Ind. Electron.*, vol. 59, no. 6, pp. 2426–2437, Jun. 2012, doi: [10.1109/TIE.2011.2169640](https://doi.org/10.1109/TIE.2011.2169640).
- [20] M. A. Benhamida, H. Ennassiri, and Y. Amara, "Reluctance network lumped mechanical & thermal models for the modeling and predesign of concentrated flux synchronous machine," *Open Phys.*, vol. 16, no. 1, pp. 692–705, Nov. 2018, doi: [10.1515/phys-2018-0088](https://doi.org/10.1515/phys-2018-0088).
- [21] R. Lin, "A design paradigm for v-shape interior permanent-magnet machines using multi-objective optimization," Ph.D. dissertation, Purdue Univ., West Lafayette, IN, USA, 2017.
- [22] J. Pyrhonen, T. Jokinen, and V. Hrabovcova, *Design of Rotating Electrical Machines*. Hoboken, NJ, USA: Wiley, 2013.
- [23] T. A. Lipo, *Introduction to AC Machine Design*. Hoboken, NJ, USA: Wiley, 2017.
- [24] V. Ostović, *The Art and Science of Rotating Field Machines Design*. Berlin, Germany: Springer, 2017.
- [25] M. S. Toulabi, J. Salmon, and A. M. Knight, "Concentrated winding IPM synchronous motor design for wide field weakening applications," *IEEE Trans. Ind. Appl.*, vol. 53, no. 3, pp. 1892–1900, May/Jun. 2017, doi: [10.1109/TIA.2017.2650985](https://doi.org/10.1109/TIA.2017.2650985).
- [26] E. C. Lovelace, T. M. Jahns, T. A. Keim, and J. H. Lang, "Mechanical design considerations for conventionally laminated, high-speed, interior PM synchronous machine rotors," *IEEE Trans. Ind. Appl.*, vol. 40, no. 3, pp. 806–812, May/Jun. 2004, doi: [10.1109/TIA.2004.827440](https://doi.org/10.1109/TIA.2004.827440).
- [27] S. Ramarathnam, A. K. Mohammed, B. Bilgin, A. Sathyan, H. Dadkhah, and A. Emadi, "A review of structural and thermal analysis of traction motors," *IEEE Trans. Transp. Electric.*, vol. 1, no. 3, pp. 255–265, Oct. 2015, doi: [10.1109/TTE.2015.2476478](https://doi.org/10.1109/TTE.2015.2476478).
- [28] D. François, A. Pineau, and A. Zaoui, *Mechanical Behaviour of Materials*. Berlin, Germany: Springer, 1998.
- [29] M. E. Gerlach, M. Zajonc, and B. Ponick, "Methodology to evaluate the mechanical stress in high-speed electric machines with buried magnets," *IEEE Trans. Ind. Appl.*, vol. 57, no. 4, pp. 3643–3653, Jul./Aug. 2021, doi: [10.1109/TIA.2021.3077527](https://doi.org/10.1109/TIA.2021.3077527).
- [30] F. Chai, Y. Li, P. Liang, and Y. Pei, "Calculation of the maximum mechanical stress on the rotor of interior permanent-magnet synchronous motors," *IEEE Trans. Ind. Electron.*, vol. 63, no. 6, pp. 3420–3432, Jun. 2016, doi: [10.1109/TIE.2016.2524410](https://doi.org/10.1109/TIE.2016.2524410).
- [31] A. Binder, T. Schneider, and M. Klohr, "Fixation of buried and surface-mounted magnets in high-speed permanent-magnet synchronous machines," *IEEE Trans. Ind. Appl.*, vol. 42, no. 4, pp. 1031–1037, Jul./Aug. 2006, doi: [10.1109/TIA.2006.876072](https://doi.org/10.1109/TIA.2006.876072).
- [32] R. Lin, S. D. Sudhoff, and C. Krousgrill, "Analytical method to compute bridge stresses in V-shape IPMs," *IET Elect. Power Appl.*, vol. 12, no. 7, pp. 938–945, Aug. 2018, doi: [10.1049/iet-epa.2018.0053](https://doi.org/10.1049/iet-epa.2018.0053).
- [33] G. Chu, R. Dutta, M. F. Rahman, H. Lovatt, and B. Sarlioglu, "Analytical calculation of maximum mechanical stress on the rotor of interior permanent-magnet synchronous machines," *IEEE Trans. Ind. Appl.*, vol. 56, no. 2, pp. 1321–1331, Mar./Apr. 2020, doi: [10.1109/TIA.2019.2960756](https://doi.org/10.1109/TIA.2019.2960756).
- [34] W. D. Pilkey, D. F. Pilkey, and Z. Bi, *Peterson's Stress Concentration Factors*. Hoboken, NJ, USA: Wiley, 2020.
- [35] G. Chu, R. Dutta, M. F. Rahman, H. Lovatt, and B. Sarlioglu, "Analytical Calculation of Maximum Mechanical Stress on the Rotor of Interior Permanent-Magnet Synchronous Machines," *IEEE Trans. Ind. Appl.*, vol. 56, no. 2, pp. 1321–1331, Mar./Apr. 2020, doi: [10.1109/TIA.2019.2960756](https://doi.org/10.1109/TIA.2019.2960756).
- [36] M. Farshadnia, R. Dutta, J. E. Fletcher, K. Ahsanullah, M. F. Rahman, and H. C. Lovatt, "Analysis of MMF and back-EMF waveforms for fractional-slot concentrated-wound permanent magnet machines," in *Proc. Int. Conf. Elect. Mach.*, Sep. 2014, pp. 1976–1982, doi: [10.1109/ICELMACH.2014.6960455](https://doi.org/10.1109/ICELMACH.2014.6960455).
- [37] M. Farshadnia, M. A. M. Cheema, R. Dutta, and J. E. Fletcher, "Analytical modeling of armature reaction air-gap flux density considering the non-homogeneously saturated rotor in a fractional-slot concentrated-wound IPM machine," *IEEE Trans. Magn.*, vol. 53, no. 2, Feb. 2017, Art. no. 8200412, doi: [10.1109/TMAG.2016.2623797](https://doi.org/10.1109/TMAG.2016.2623797).
- [38] Q. Li, T. Fan, and X. Wen, "Armature-reaction magnetic field analysis for interior permanent magnet motor based on winding function theory," *IEEE Trans. Magn.*, vol. 49, no. 3, pp. 1193–1201, Mar. 2013, doi: [10.1109/TMAG.2012.2224358](https://doi.org/10.1109/TMAG.2012.2224358).
- [39] Q. Chen, G. Xu, G. Liu, W. Zhao, L. Liu, and Z. Lin, "Torque ripple reduction in five-phase IPM motors by lowering interactional MMF," *IEEE Trans. Ind. Electron.*, vol. 65, no. 11, pp. 8520–8531, Nov. 2018, doi: [10.1109/TIE.2018.2807392](https://doi.org/10.1109/TIE.2018.2807392).
- [40] N. Bianchi, S. Bolognani, D. Bon, and M. Dai Pre, "Torque harmonic compensation in a synchronous reluctance motor," *IEEE Trans. Energy Convers.*, vol. 23, no. 2, pp. 466–473, Jun. 2008, doi: [10.1109/TEC.2007.914357](https://doi.org/10.1109/TEC.2007.914357).
- [41] A. Ebrahimi, "A contribution to the theory of rotating electrical machines," *IEEE Access*, vol. 9, pp. 113032–113039, 2021, doi: [10.1109/ACCESS.2021.3104013](https://doi.org/10.1109/ACCESS.2021.3104013).
- [42] M. Xu, G. Liu, Q. Chen, J. Ji, and W. Zhao, "Torque calculation of stator modular PMA-SynRM with asymmetric design for electric vehicles," *IEEE Trans. Transp. Electric.*, vol. 7, no. 1, pp. 202–213, Mar. 2021, doi: [10.1109/TTE.2020.3007394](https://doi.org/10.1109/TTE.2020.3007394).
- [43] A. Arzillo et al., "Challenges and future opportunities of hairpin technologies," in *Proc. IEEE 29th Int. Symp. Ind. Electron.*, Jun. 2020, pp. 277–282, doi: [10.1109/ISIE45063.2020.9152417](https://doi.org/10.1109/ISIE45063.2020.9152417).
- [44] A. Boglietti, A. Cavagnino, M. Lazzari, and M. Pastorelli, "A simplified thermal model for variable-speed self-cooled industrial induction motor," *IEEE Trans. Ind. Appl.*, vol. 39, no. 4, pp. 945–952, Jul./Aug. 2003, doi: [10.1109/TIA.2003.814555](https://doi.org/10.1109/TIA.2003.814555).
- [45] P. H. Mellor, D. Roberts, and D. R. Turner, "Lumped parameter thermal model for electrical machines of TEFC design," *IEE Proc. B, Elect. Power Appl.*, vol. 138, no. 5, pp. 205–218, 1991, doi: [10.1049/ip-b.1991.0025](https://doi.org/10.1049/ip-b.1991.0025).
- [46] F. Graffeo, S. Vaschetto, A. Miotto, F. Carbone, A. Tenconi, and A. Cavagnino, "Lumped-parameters thermal network of PM synchronous machines for automotive brake-by-wire systems," *Energies (Basel)*, vol. 14, no. 18, Sep. 2021, Art. no. 5652, doi: [10.3390/en14185652](https://doi.org/10.3390/en14185652).
- [47] S. Vaschetto, A. Tenconi, and G. Bramerdorfer, "Sizing procedure of surface mounted PM machines for fast analytical evaluations," in *Proc. IEEE Int. Electric Machines Drives Conf.*, May 2017, pp. 1–8, doi: [10.1109/IEMDC.2017.8002223](https://doi.org/10.1109/IEMDC.2017.8002223).
- [48] A. Boglietti, A. Cavagnino, and M. Lazzari, "Computational algorithms for induction-motor equivalent circuit parameter determination—Part I: Resistances and leakage reactances," *IEEE Trans. Ind. Electron.*, vol. 58, no. 9, pp. 3723–3733, Sep. 2011, doi: [10.1109/TIE.2010.2084974](https://doi.org/10.1109/TIE.2010.2084974).
- [49] A. Boglietti, A. Cavagnino, and M. Lazzari, "A recursive algorithm to resolve the skin effects in rotor bars of squirrel cage induction motor," in *Proc. Int. Conf. Elect. Mach.*, 2004, pp. 394–400.



MOSTAFA AHMADI DARMANI received the Ph.D. degree in electrical engineering from Politecnico di Torino, Torino, Italy, in 2022.

He is currently a Research Fellow in electrical machines with the Power Electronics Drive Control group, University of Nottingham, Nottingham, U.K. His main research interests include the multiphysics design and analysis of high-performance electrical machines, design of magnetic components for high-frequency power conversion, and advanced materials for electromechanical energy

conversion systems.

Dr. Darmani is a reviewer for several IEEE Transactions and international journals and conferences.



ANDREA CAVAGNINO (Fellow, IEEE) was born in Asti, Italy, in 1970. He received the M.Sc. and Ph.D. degrees in electrical engineering from the Politecnico di Torino, Torino, Italy, in 1995 and 2000, respectively.

He is a Professor with the Politecnico di Torino. He has authored or coauthored more than 250 papers. His research interests include electromagnetic design, thermal design, and energetic behavior of electrical machines. He usually cooperates with factories for a direct technological transfer,

and he has been involved in several public and private research projects.

Dr. Cavagnino was the recipient of four Best Paper Awards. He is an Associate Editor of IEEE TRANSACTIONS ON ENERGY CONVERSION, a Past Chair of the Electrical Machines Technical Committee of the IEEE Industrial Electronics Society, a past Associate Editor of IEEE TRANSACTIONS ON INDUSTRIAL ELECTRONICS, and IEEE TRANSACTIONS ON INDUSTRY APPLICATIONS. He was also a Guest Editor of six Special Sections for IEEE-TIE and Co-Editor in Chief of a Special Issue for IEEE-TEC. He was a Technical Program Chair of the IEEE-IEMDC 2015 and IEEE-ECCE 2022 conferences. He is a reviewer for several IEEE Transactions and other international journals and conferences.



SILVIO VASCETTO (Senior Member, IEEE) received the M.Sc. and Ph.D. degrees in electrical engineering from the Politecnico di Torino, Torino, Italy, in 2007 and 2011, respectively.

He then joined ABB IEC LV Motors Technology Center, Vittuone, Italy, as an R&D engineer. From 2012 to 2014, he was with Magna Electronics Italy, as Electromagnetic Simulation and Motor Design Engineer. He is currently an Associate Professor with the Energy Department “G. Ferraris,” Politecnico di Torino. His research interests include

electromagnetic design, thermal analysis, and energetic behavior of electrical machines for transportations and high-performance applications.

Dr. Vaschetto is an Associate Editor for IEEE TRANSACTIONS ON INDUSTRY APPLICATIONS, IEEE TRANSACTIONS ON ENERGY CONVERSION, and Special Issues Editor for *IET Electric Power Applications Journal*.



FABRIZIO MARIGNETTI (Senior Member, IEEE) received the Laurea (Hons.) and the Ph.D. degrees in electrical engineering from the University of Naples Federico II, Naples, Italy, in 1993 and 1998, respectively.

In 1998, he joined the University of Cassino, Italy, where he is a Full Professor of power electronic converters, electrical machines and drives. His research interests include the design, analysis, and digital control of electrical machines, renewable energies, and power converters. In 2009, he

founded the spin-off company LEDA Srl, Laboratory of Advanced Electro-Dynamics, of which he is a Member of the Executive Board. He has authored or coauthored 300 publications in his research field and the inventor of five patents

Dr. Marignetti has been the Chair of the Industrial Electronics Chapter of the IEEE Italy Section since 2022. Since 2015, he has been a Fellow of the National Institute of Nuclear Physics. He won five paper awards. Since 2021, he has been a Member of CIGRE Workgroup WG C4.61 Lightning transient sensing, monitoring and application in electric power systems and a Member of the Executive Board of the EnSiEl Consortium of Energy and Electrical Systems.



CHRISTOPHER GERADA (Senior Member, IEEE) received the Ph.D. degree in numerical modeling of electrical machines from the University of Nottingham, Nottingham, U.K., in 2005.

Subsequently, he was a Researcher with the University of Nottingham, on high-performance electrical drives and on the design and modeling of electromagnetic actuators for aerospace applications. Since 2006, he has been the Project Manager of the GE Aviation Strategic Partnership.

He was appointed as a Lecturer of electrical machines in 2008, an Associate Professor in 2011, and a Full Professor in 2013 with the University of Nottingham, in 2005. His core research interests include the design and modelling of high-performance electric drives and machines. He established and is the Director of the Cummins Innovation Centre and has also led several major research consortiums and centers (GE Aviation UTSP, FIRST-Advance Propulsion Centre, Actuation2015). He has secured >£60M of research income as PI and has a very strong track record of industrial engagement through industrial projects and consultancies.

Dr. Gerada holds a prestigious Royal Academy of Engineering Chair in Electrical Machines, is also the past Chair of the IEEE Industrial Electronics Society Electrical Machines Technical Committee and an Associate Editor for IEEE TRANSACTIONS IN INDUSTRY APPLICATIONS.